Direct observation of anisotropic small-hole polarons in an orthorhombic structure of BiVO₄ films

A. Chaudhuri,[1,2] L. Mandal,[1] X. Chi,[2,3] M. Yang,[4,5] M. C. Scott,[6] M. Motapothula,[1] X. J. Yu,[2] P. Yang,[2] Y. Shao-Horn,[7] T. Venkatesan,[1,3,8,9,*] A. T. S. Wee,[3,5,8,†] and A. Rusydi[1,2,3,5,8,‡]

[1]*NUSSNI-NanoCore, National University of Singapore, Singapore 117576, Singapore*
[2]*Singapore Synchrotron Light Source, National University of Singapore, 5 Research Link, Singapore 117603, Singapore*
[3]*Department of Physics, National University of Singapore, Singapore 117542, Singapore*
[4]*Institute of Materials Research and Engineering, A*STAR, 2 Fusionopolis Way, Singapore 138634, Singapore*
[5]*Centre for Advanced 2D Materials and Graphene Research Centre, National University of Singapore, Singapore 117546, Singapore*
[6]*Department of Materials Science and Engineering, University of California, Berkeley, California 94720, USA*
[7]*Electrochemical Energy Laboratory, Massachusetts Institute of Technology, 77 Massachusetts Avenue, Cambridge, Massachusetts 02139, USA*
[8]*National University of Singapore Graduate School for Integrative Sciences and Engineering (NGS), 28 Medical Drive, Singapore 117456, Singapore*
[9]*Department of Materials Science and Engineering, National University of Singapore, Singapore 117583, Singapore*

Here, we report an anisotropic small-hole polaron in an orthorhombic structure of BiVO₄ films grown by pulsed-laser deposition on yttrium-doped zirconium oxide substrate. The polaronic state and electronic structure of BiVO₄ films are revealed using a combination of polarization-dependent x-ray absorption spectroscopy at V $L_{3,2}$ edges, spectroscopic ellipsometry, x-ray photoemission spectroscopies, and high-resolution x-ray diffraction with the support of first-principles calculations. We find that in the orthorhombic phase, which is slightly different from the conventional pucherite structure, the unoccupied V *3d* orbitals and charge inhomogeneities lead to an anisotropic small-*hole* polaron state. Our result shows the importance of the interplay of charge and lattice for the formation of a hole polaronic state, which has a significant impact in the electrical conductivity of BiVO₄, hence its potential use as a photoanode for water splitting.

I. INTRODUCTION

Bismuth vanadate (BiVO₄) has been a subject of interest for decades due to its rich fundamental properties and a wide range of applications, including, for example, the commercial use as a nontoxic yellow pigment [1,2], degrading agent for organic contaminants (dye) under ultraviolet or visible light irradiation [3], gas sensor [4], and in solid-oxide fuel-cell applications [5,6]. Other unique properties, viz, ferroelasticity [7], photochromic effects [8], and ionic conductivity [9] of the material, have also attracted intensive research interest. Recently, BiVO₄ was found to be a promising solar-light-driven photocatalyst owing to its moderate band-gap energy, which is ideal for both ultraviolet and visible light absorption [10,11]. In addition, the well-positioned band-edge alignment with respect to water redox potential [12] has made BiVO₄ an attractive candidate as a photoanode for photoelectrochemical (PEC) water splitting by utilizing the solar energy for producing H₂ and O₂ as alternative fuels [13,14]. However, the solar-to-hydrogen conversion efficiency of BiVO₄ is significantly lower compared to the theoretical value, which is ascribed to the poor charge transport of the material and limits its application

as a photoanode in practice [15,16]. It has been theoretically predicted that charge localization might result in the formation of small polarons, thereby restricting the charge mobility [17]. Instead of moving freely, the charges are forced to hop via V sites of the lattice; this hopping motion of electron is considered as the principal cause of the low electrical conductivity [17,18]. However, this explanation for the low charge transport has not yet been substantiated, as no direct evidence of polaron formation has been reported for pristine BiVO₄. The possibility of polaron formation and their contribution in charge transport remains a critical issue in BiVO₄ for the PEC application. Here we present direct evidence of anisotropic small-hole polaron formation in an orthorhombic phase of pristine BiVO₄ using polarization-dependent x-ray absorption spectroscopy along with spectroscopic ellipsometry, and corroborate the results with x-ray photoemission spectroscopy and high-resolution x-ray diffraction as well as theoretical calculations of a distinctive polaronic state.

The photocatalytic activity of BiVO₄ is believed to be strongly influenced by the crystal phases [19,20], facets [21], and bond distortions. The structural unit of BiVO₄ consists of VO₄ tetrahedra and BiO₈ dodecahedra [22,23], which are connected to each other via an apex oxygen atom. The distortion of the polyhedra in BiVO₄ structures affects the photocatalytic property [24]. Monoclinic BiVO₄, with a band gap energy of 2.4-2.5 eV, has been reported to show higher efficiency as a photo-catalyst, especially, in water splitting and

*venky@nus.edu.sg
†phyweets@nus.edu.sg
‡phyandri@nus.edu.sg

O_2 evolution reactions compared to the polymorphs [20,24,25]. Hence, studies have been mainly performed to synthesize, characterize, and explore the fundamental properties of monoclinic $BiVO_4$; while reports on the other phases are limited. It remains challenging, so far, to synthesize the orthorhombic structure [7].

In this paper, we report the orthorhombic $BiVO_4$ thin film grown on yttrium-doped zirconium oxide (YSZ) substrate via pulsed-laser deposition method. Synchrotron-based high-resolution x-ray diffraction (HR-XRD) measurements, polarization-dependent x-ray absorption spectroscopy (XAS), and reflective spectroscopic ellipsometry (SE) have been carried out as the part of the experiments to characterize the crystal and the electronic structures in detail with the support of the first-principles calculation (density-functional theory, DFT). The crystal phase, structure, and unit-cell parameters are precisely determined by HR-XRD [26]. The polarization-dependent XAS is employed at the V $L_{3,2}$ edges to probe the electronic structure and the orbital splitting of the V *3d* states. The observed XAS is directly compared to the DFT calculations to assign the unoccupied *d* orbitals near the conduction-band minimum. A new prepeak is experimentally observed at the V L_3 edge, and its origin is explained by the DFT calculations obtained from the orthorhombic structure using the lattice parameters evaluated by HR-XRD. The SE measurement shows an optical transition just below the absorption edge, hence confirming the existence of the hole polaronic states.

II. EXPERIMENT

A. Sample preparation (pulsed-laser deposition)

YSZ ($a = 5.145$ Å) has an excellent lattice match with the base of the unit cell of monoclinic $BiVO_4$ ($a = 5.1956$ Å, $b = 5.0935$ Å) [27]. In our present work, a high-quality orthorhombic phase of $BiVO_4$ (thickness $\sim$750 nm) is grown epitaxially on cubic YSZ substrate via the pulsed-laser deposition method. Note that there was an earlier report of monoclinic structure formation (thickness $\sim$65 nm) on this substrate [28]. The ceramic targets are made using Bi_2O_3 and V_2O_5 (99.99%) pure nanopowder by solid-state reaction. The target composition and laser fluence (2 J/cm^2) are kept constant throughout the film growth. Depositions are carried out under the condition of 80 mJ per laser pulse at 2 Hz, 600 ˚C substrate temperature, and 100-mbar oxygen partial pressure.

B. High-resolution x-ray diffraction

The film is characterized by HR-XRD in the x-ray demonstration and development beam line at Singapore Synchrotron Light Source (SSLS). The detailed description of the beam line is reported elsewhere [29]. A monochromatic x-ray beam, with photon energy close to Cu-Kα line (8.111 keV), is used for HR-XRD measurement. The data for HR-XRD reciprocal-space mappings (RSMs) were collected under the framework of an (*hkl*) coordinate system with precision better than 0.5/1,000 in reciprocal lattice units. The coordinates of three selected reciprocal-space vectors, for both substrates and films, are measured during data collection or read from RSMs; these are used to determine the crystal system and to calculate its lattice parameters. The coordinate system with respect to the substrate is used.

C. X-ray absorption spectroscopy

XAS measurements were carried out at the Surface, Interface and Nanostructure Science (SINS) beam line, SSLS. Details of the beam line are described elsewhere [30]. The V *L*-edge absorption data are collected in total electron yield (TEY) mode monitoring total current. The base pressure in the UHV chamber is maintained at $\sim$2 × 10^{-10} mbar throughout the measurements. The collected V L_3 XAS spectra are normalized by the incident photon flux (I_0) and fitted with a Shirley background subtraction and Voigt line shapes for the peaks.

D. Spectroscopic ellipsometry

Spectroscopic ellipsometric parameters Ψ and Δ (viz., the ratio of the amplitude and phase difference between *p*-and *s*-polarized reflected light, respectively) are collected at 70˚ angle of incidence, with a photon energy range between 1 and 5 eV using a Woollam V-VASE ellipsometer. Details of the instrument and measurement geometry are described elsewhere [31]. The real and imaginary parts of the dielectric constant ($\tilde{\varepsilon}_1$ and $\tilde{\varepsilon}_2$) are derived from the measured values of the parameters Ψ and Δ, using Woollam COMPLETE EASE software.

E. X-ray photoelectron spectroscopy

The x-ray photoelectron spectra (XPS) measurements are performed at room temperature using a monochromatized Al K$_\alpha$ x-ray radiation source ($hv = 1486.6$ eV, linewidth 0.85 eV), on a Krotos Axis ultra DLD system. The base pressure is maintained below 10^{-9} mbar during measurements. The energy scale of the spectrometer has been calibrated with standard Ag $3d_{5/2}$ samples. $C 1s = 284.6$ eV as a reference criterion is used to correct the charge effect. CASA XPS analysis software is used for the spectral fitting.

III. COMPUTATIONAL DETAILS

All spin-polarized calculations were performed by using the DFT-based Vienna *Ab initio* Simulation Package (VASP 5.4.1) [32,33] with the generalized gradient approximation (GGA) functional in Perdew-Burke-Ernzerhof format and the projector augmented wave potentials [34,35]. A cutoff energy of 500 eV was set for the electronic plane-wave expansion. A Γ-centered $9 \times 8 \times 3$ *k*-point mesh was used to sample the first Brillouin zone of the orthorhombic $BiVO_4$ unit cell. The total energy and force on each atom were converged to 10^{-6} eV and 0.01 eV/Å, respectively. In this study, the generalized gradient approximation (GGA) with Hubbard correction (U) (GGA+U) method based on Dudarev's scheme with an effective Hubbard $U_{\text{eff}} = 2.25$ eV was applied to the *d* orbital of vanadium atoms in order to take into account the orbital-dependent Coulomb and exchange interaction [36].

A $2 \times 2 \times 1$ orthorhombic $BiVO_4$ supercell was adopted to calculate the electron polarons, in which the Brillouin zone was sampled by a $5 \times 4 \times 3$ *k*-point mesh. To create the polaronic state, we introduce one excess electron in the supercell, and apply a small distortion to a selected V atom to break lattice
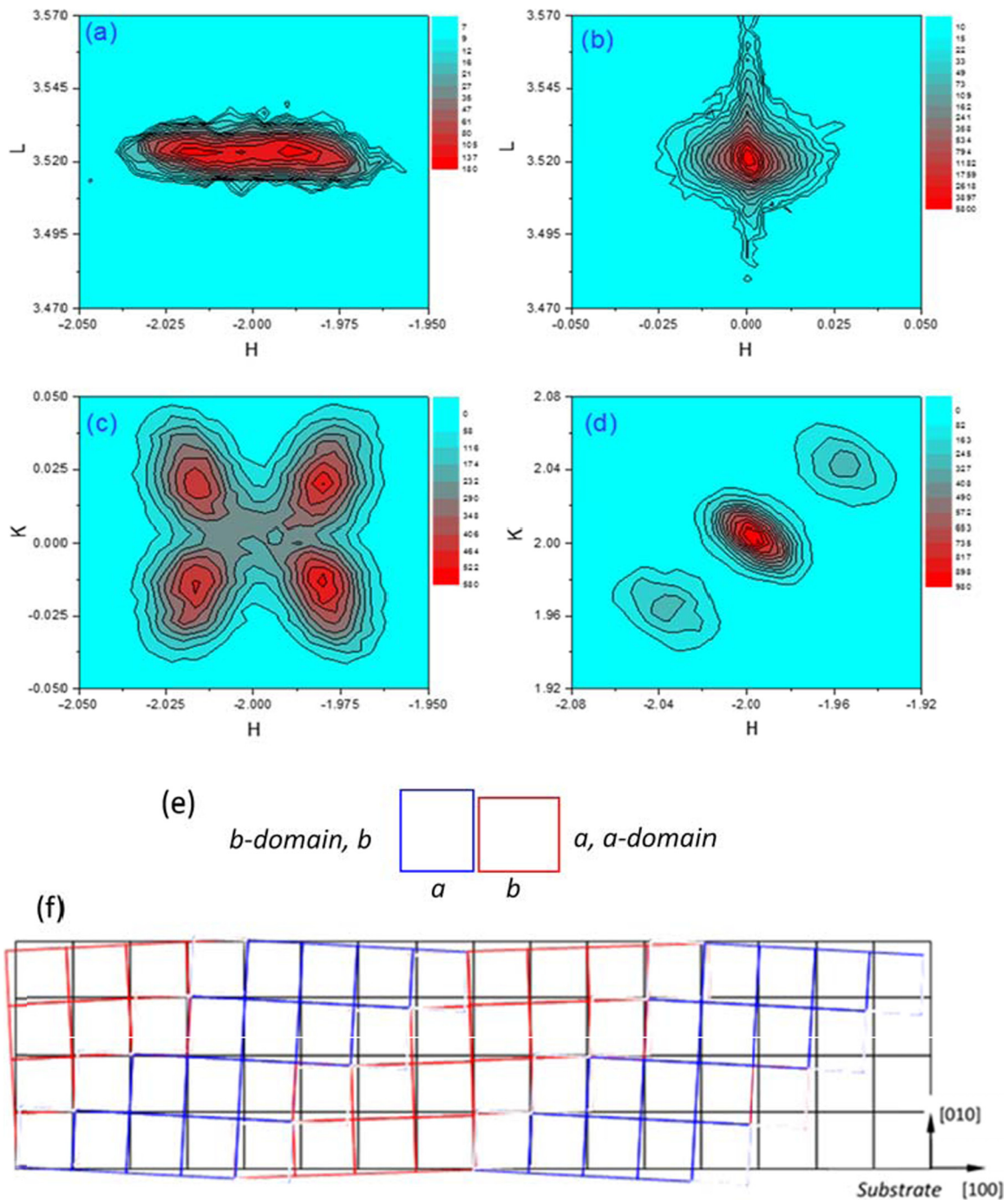
FIG. 1. RSMs for BiVO$_4$ showing the twin variants in reciprocal space. L value denotes the height of the central spot at the L axis. (a) (-204) hl mapping for the film: $L = 3.521$; (b) (004) hl mapping for the film: $L = 3.521$; (c) (-204) hk mapping for the film: $L = 3.521$; (d) (-224) hk mapping for the film: $L = 3.521$; (e) blocks of a- and b domain; (f) formation of twist lattice network in film parallel to the substrate.

symmetry before the structural optimization. We also consider a nonpolaronic state, in which the excess electron is introduced into the supercell but without the initial perturbation on the V atom.

IV. RESULTS AND DISCUSSION

The RSM precisely determines the unit-cell parameters and confirms the existence of the orthorhombic phase with twin

formation. The lattice parameters are determined as $a = 5.104 \pm 0.003$ Å, $b = 5.191 \pm 0.001$ Å, and $c = 11.693 \pm 0.001$ Å. Interestingly, the average diagonal length of the lattices in the ab plane is 7.276 Å, close to 7.278 Å of the YSZ substrate. This is significant to judge the reasonableness of twin formation. The twin variants are shown in reciprocal space (Fig. 1). There is only one concentrated spot in (004) hl mapping in Fig. 1(b), which indicates that the twin variants are all aligned along the (001) plane without any tilting. There

are fourfold-distributed spots in the (-204) *hk* mapping in Figs. 1(c) and 1(a), implying that there are two lengths for in-plane axes of *a* and *b*. Further, (-224) *hk* mapping shows that the lengths of all spots are the same in the RSM, i.e., there is no more than one *d*-spacing of {110} type, which implies the angle between the in-plane *a* axis and *b* axis is 90°. This confirms that the crystal system of the lattice is orthorhombic. The peaks in (-224) *hk* mapping show the same spacing of four twin variants of {−220} type (the distances are the same to the origin), the twist lattice illustrated in Fig. 1(f). The central peak is formed with two of the variants overlapped and another two formed with misorientation due to the twist lattice in film. A schematic of twin formation in the *ab* plane, blocks of *a* domain, *b* domain ($a \neq b$), and the model of lattice network in film parallel to the substrate are proposed, respectively, in Figs. 1(e) and 1(f). The boundary between the substrate and the film forms a kind of twist boundary. Choosing the spots in Fig. 1(c) and using $a = 5.104$ Å and $b = 5.191$ Å for *a*- and *b* domains, respectively, the mutual angles of the domains are matching each other, around 0.97°.

The V *L*-edge XAS originates from the transition of electrons from V $2p$ core level to the unoccupied V $3d$ bands. The spectrum splits into two well-defined L_3 and L_2 white-line regions centered at $\sim$518 and $\sim$525 eV, respectively. Considering the *j-j* coupling scheme and dipole selection rule, these regions can be attributed to transitions from the inner $2p$ shell of the V atom to the empty $3d$ states, i.e., V $2p_{3/2} \rightarrow$ V $3d$ and V $2p_{1/2} \rightarrow$ V $3d$. The separation between the L_3 and L_2 region in the spectrum, the spin-orbital splitting ($\sim$6.9 eV), defines the splitting of the $2p$ core level of the V atom. Our observed value is slightly higher than that (6.6 eV) of the previously reported value for the monoclinic structure [37], implying a slightly different degree of distortion in the V tetrahedral unit than that of the monoclinic structure. The V L_3 and L_2 peaks have their own characteristic broadening. For the early $3d$ transition metals like V, there is some overlap between these two regions and the separation is not distinct. The L_2 edge, which is due to the transition from the $p_{1/2}$ states, also contains the Coster-Kronig Auger decay process [38]. As a result, the peak is broadened and sometimes there are losses from the main line intensities to satellite structures [39]. Hence, the V L_2 edge is rather complex in terms of elucidating the electronic structure of the VO$_4$ tetrahedron unit within BiVO$_4$.

The V L_3-edge spectrum is a fingerprint of the *d*-projected unoccupied density of states. Multiplet effects and crystal-field splitting dominate the features of the spectrum, and it is sensitive to site symmetry and oxidation states as well [40,41]. Figure 2(a) displays the V L_3 absorption edge, taken at normal incidence, enabling the polarization vector of the incident radiation to be perpendicular to the surface normal. To evaluate the specific multiplet states associated with the *p-d* orbital interactions, the XAS spectrum at the V L_3 edge is deconvoluted into four components at 515.9 ± 0.01, 516.9 ± 0.01, 518 ± 0.01, and 518.7 ± 0.02 eV and are compared with the energy states obtained from the computed partial density of states (described later) of the orthorhombic structure under consideration. The tetrahedral crystal field splits the V L_3 spectrum into two distinct energy states "*e*" (contains doubly degenerate states $3d_{x^2-y^2}$ and $3d_{z^2}$) and t_2 (contains
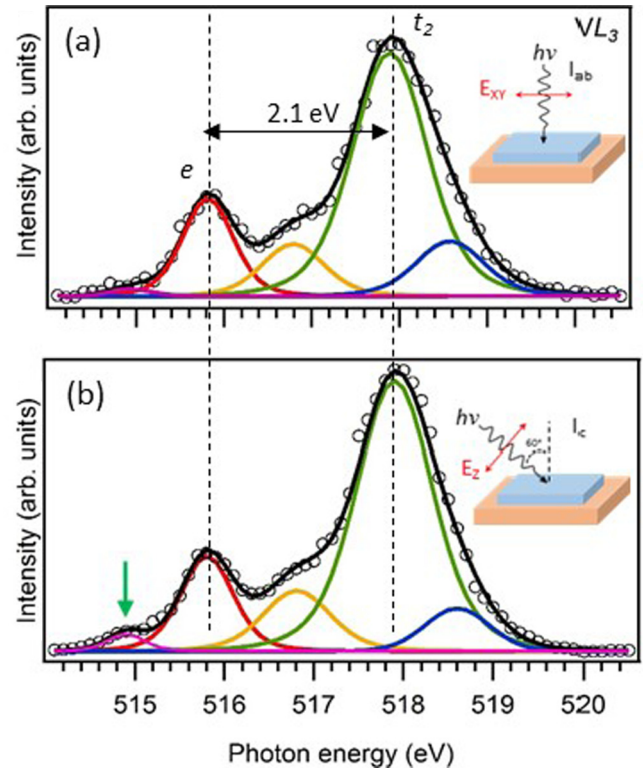

FIG. 2. X-ray absorption spectra of orthorhombic BiVO$_4$ measured in TEY mode at the V L_3-edge absorption edge (a) at normal incidence, (b) at grazing incidence. Data points are shown as empty circles. The spectral fits (continuous black line) are made up of the sum of individual component peaks (colored traces). The distinct prepeak is shown by green arrow in (b).

triply degenerate states $3d_{xy}$, $3d_{yz}$, and $3d_{xz}$), around 515.9 ± 0.01 and 518 ± 0.01 eV, respectively. The separation between the two states, i.e., the so-called "10 *Dq*" value is 2.1 eV, which is comparable with 2.12 eV of monoclinic BiVO$_4$ [37]. A close comparison with the DFT calculations suggests that the peak at 515.9 eV corresponds to the *e* state, where the $3d_{x^2-y^2}$ orbital is pushed up to higher energy and the $3d_{z^2}$ orbital mainly dominates the conduction band edge similar to that observed in the case of monoclinic structure [42]. The multiplet at 516.9 eV, within the t_2 region, exhibits a combined character of d_{yz} and d_{xz} orbitals, whereas the peak around 518.0 eV arises mainly from the transitions associate with d_{xy} and d_{yz} multiplets. The precise evaluation of the peak around 518.7 eV remains uncertain as the spectral feature in this region can be suppressed and distorted by the contribution from the L_2 edge.

Our significant observation is a prepeak close to the absorption edge around 514.9 ± 0.14 eV of the V L_3 XAS spectrum, which is about $\sim$0.9 eV below the conduction band. Note that this prepeak was absent in monoclinic BiVO$_4$ [37]. Interestingly, the prepeak becomes clearly noticeable and distinct when the spectrum is collected at a grazing angle with the polarization vector of the incident radiation at 60° relative to the surface normal [see Fig. 2(b)]. Thus, we observe an anisotropic character of the prepeak with respect to the polarization of the incident photon beam, similar to that reported for the tungsten-doped monoclinic BiVO$_4$
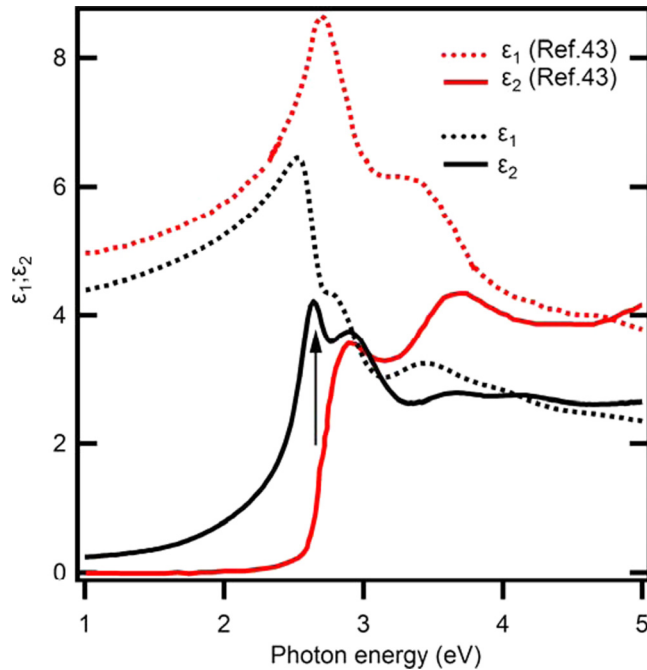
FIG. 3. Real part (ε_1) and imaginary part (ε_2) of dielectric function of the orthorhombic BiVO$_4$ thin film obtained by spectroscopic ellipsometry. For comparison, reported ε_1 and ε_2 for the monoclinic BiVO$_4$ [43] are included.

structure [18], confirming the transition is more likely arising from bulk, rather than a surface effect.

In Fig. 3, we compare the dielectric functions of our orthorhombic BiVO$_4$, obtained from the spectroscopic ellipsometry, with that of the monoclinic BiVO$_4$ [43]. A clear peak (indicated by the vertical arrow) in the imaginary part (ε_2) of the dielectric function at around 2.55 eV is observed in the orthorhombic BiVO$_4$, nearly 0.26 eV below the absorption edge of the monoclinic BiVO$_4$. The appearance of distinct transition just below the optical absorption edge strongly suggests existence of a polaronic state. Together with XAS, which probes unoccupied states, we confirm that the peak is a hole polaronic state.

Although the experimental evidence for the existence of the polaronic state from the V L_3 XAS spectra has not been reported so far; the polaronic satellites were observed in the L-edge absorption spectra for different oxide phases of TiO$_2$ [44]. Note that previous study has shown the presence of small electron polaronic states in Li$_x$V$_2$O$_5$ nanowires using hard x-ray photoemission spectroscopy measurements [45]. The formation of a polaronic state is attributed mainly to the charge transfer due to V^{5+} to V^{4+} oxidation states resulting a local lattice distortion around the V^{4+} site. The oxidation state of the BiVO$_4$ sample is verified by the V $2p$ XPS (shown in Fig. 4). The V $2p_{3/2}$ (at 516.8 eV) and V $2p_{1/2}$ (at 524.6 eV) peaks are separated by a spin-orbit split of 7.8 eV in 2:1 peak ratio, typical for V^{5+} oxidation state. The weak shoulder at the 515.7 eV of V $2p_{3/2}$ and 523.4 eV of V $2p_{1/2}$ may be attributed to V^{4+} states; however, it remains challenging to quantify it precisely.

To have further support for our experimental results, the partial density of states is calculated. The optimized structure
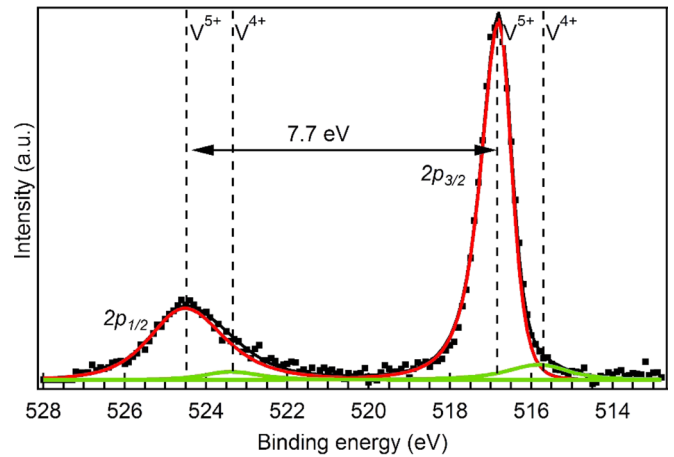

FIG. 4. X-ray photoelectron spectra of V $2p_{3/2}$ for BiVO$_4$ sample under consideration. (Solid dots: experimentally observed data. Solid lines: fitted curves, red: V^{5+}, green: V^{4+}).

and the electronic properties of the orthorhombic BiVO$_4$ unit cell are shown in Fig. 5, in which the lattice parameters are $a = 5.10$ Å, $b = 5.38$ Å, and $c = 12.06$ Å; and an indirect band gap with a value of 2.55 eV is noted. This calculated band gap is comparable with 2.48 eV of monoclinic BiVO$_4$ due to similar bonding character in these two phases [37,42]. Figure 6(a) shows the projected density of states of the orthorhombic BiVO$_4$, from which we can see that the valence-band maximum is mainly contributed by the O $2p$ orbital that hybridizes with V $3d$ and Bi $6s$ orbitals. The conduction-band minimum is predominantly composed of the antibonding states of V $3d$ orbital, as well as weak contribution from O $2p$ and Bi $6p$ orbitals. It is found that the crystal field of VO$_4$ tetrahedron in the orthorhombic BiVO$_4$ lifts the V $3d$ orbital degeneracy and shifts the e states toward lower energy. Further, the suppression in the z direction causes a further splitting in e states, leading to a dominant $3d_{z^2}$ orbital in the conduction-band minimum, as shown in Fig. 6(b).

The excess electrons in oxides can either retain free-electron character (nonpolaron state), or interact with the host lattices strongly, forming a polaronic state [46]. For an excess electron in the orthorhombic BiVO$_4$, we find that the formation of the polaronic state is favorable as the energy of polaronic state is
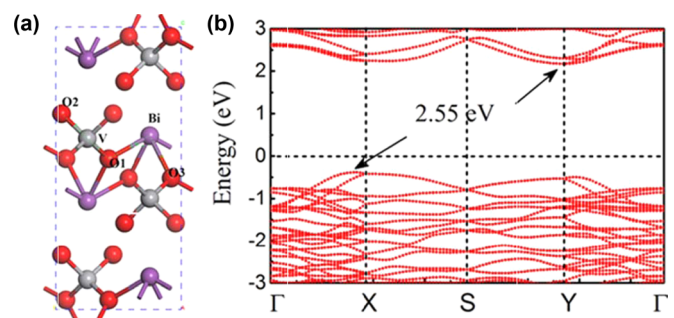

FIG. 5. (a) Atomic structure of the optimized orthorhombic BiVO$_4$ unit cell and (b) the corresponding band structure. The Fermi level is shifted to 0 eV.
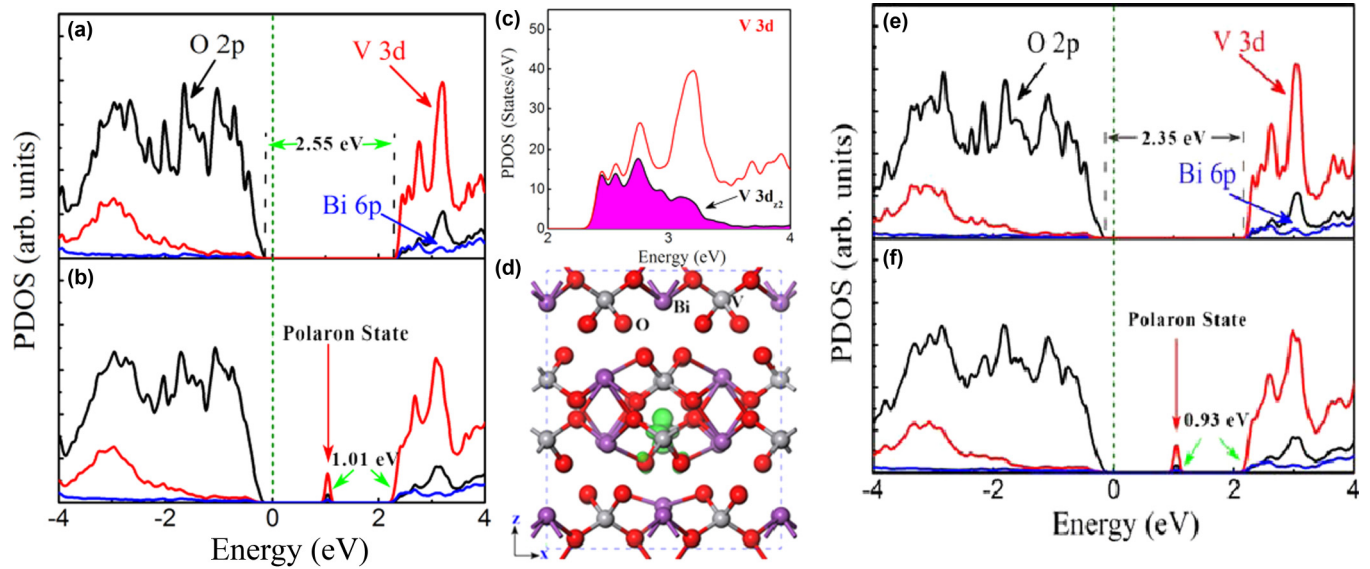
FIG. 6. PDOS of BiVO$_4$ supercell without an excess electron. (a) PDOS of BiVO$_4$ supercell and (b) the PDOS projected on V $3d_{z^2}$ at the conduction-band edge of the BiVO$_4$ supercell, which clearly shows small-hole polaronic state. (c) The PDOS of BiVO$_4$ with an excess electron and (d) the visualized partial charge density at the energy position of the polaron state with an isosurface value of 1.0×1.0^{-3} e/Å^3. The Fermi energy is shifted to 0 eV. (e) The PDOS of BiVO$_4$ supercell with 3.4% strain. (f) The PDOS of BiVO$_4$ supercell with 3.4% strain and an excess electron.

about 418 meV lower than that of the nonpolaronic state. It turns out that the electron will localize at the vanadium site, filling up the lowest unoccupied states, $3d_{z^2}$ state of the V $3d$ orbital, and reducing the valence state V^{5+} to V^{4+}. This strong electron-phonon interaction results in significant local lattice distortion, as suggested by about 0.12-Å elongation of the V^{4+}−O bond in the polaron state compared with the V^{5+}−O bond in the nonpolaronic state. The filled $3d_{z^2}$ state is split from the antibonding states of the V $3d$ orbital and moves toward lower energy, forming a localized state shown in the partial density of states (PDOS) [Fig. 6(c)], which is about 1.01 eV below the conduction-band edge. Due to the orbital hybridization, the weak contribution from the O $2p$ orbital can also be seen in the polaronic state. The visualized partial charge density of the polaronic state is shown in Fig. 6(d). The dominant charge density with a character of d_{z^2} state is localized at the distorted vanadium ions, as well as weakly contributed from its neighbor O ions, consistent with the calculated PDOS.

Since the orthorhombic BiVO$_4$ thin films is epitaxially grown on YSZ substrate, about 3.4% compressive strain is expected along the y direction of the films; as a result, the lattice parameter "b" is modified to 5.191 Å, as observed by HR-XRD. This compressive strain slightly reduces the band gap to 2.35 eV [see Fig. 6(e)]. We find that the polaronic state remains stable at this strain as shown in Fig. 6(f), but its peak position in the PDOS is about 0.93 eV below the conduction edge, in good line with the 0.9 eV observed in the XAS spectroscopy. Although, the compressive strain of 3.4% is rather high and is not corrected for the temperature effect, we notice the modification of the polaronic peak position will remain nearly unaltered. More importantly, comparing with the DFT results, the complex dielectric functions from

spectroscopic ellipsometry measurement show that the polaron peak as well as the optical band gap occur at higher energies than our theoretical calculations. This reveals the importance of electron-electron interaction in the formation of polaron in the optical response. It is known that the electron-electron interactions push the spectral weights toward higher energies [47] as we observe for the orthorhombic BiVO$_4$ thin film in this study.

Nevertheless, our experimental data, with the support of DFT calculation, suggest that formation of the small-hole polaronic state, which is due to the interplay of charge and lattice, is intrinsic for the pristine BiVO$_4$ phase under consideration. Oxygen vacancies, which often exist particularly in thin films and are typical for the transition-metal oxides like V, may provide the extra electrons to the system and these electrons are localized to the V^{5+} sites reducing the charge to V^{4+}, measured weakly by XPS. We note that it is challenging, though, to quantify the oxygen vacancies. By combining XAS and SE results with the DFT calculations, we conclude that a hole polaronic state exists at the bottom of the conduction band. This polaronic state exhibits a spatial anisotropic character with a peak width which is wider in the ab plane compared to the c axis. The origin of the anisotropy of the bulk electronic conductivity of BiVO$_4$ (the dc electrical conductivities measured in the ab plane are higher than that along the c axis) [18,48] may be viewed through the spatial anisotropic nature of the polaronic state.

V. CONCLUSIONS

In conclusion, the electronic structure of the orthorhombic BiVO$_4$ film, which closely resembles that of the monoclinic BiVO$_4$ structure, shows a highly anisotropic small-hole

polaronic state just at the edge of the conduction band. As supported by the theoretical calculations, this polaronic state of the orthorhombic structure is contributed by the vanadium oxidation states ranging from V^{5+} to V^{4+} resulting in local lattice distortions of VO_4 tetrahedral symmetry. Our study explicitly supports the formation of polarons in $BiVO_4$, an important visible-light photocatalyst. Thereby, the role of this polaronic state as a "charge trap" due to its close proximity to the band edge leading to the poor performance for the water splitting, can be explained at the fundamental level from this study. Our results may open up new strategies to mitigate the detrimental effect of polarons in the performance of $BiVO_4$ in photocatalytic applications and the methodology presented to probe polaronic states can be used to other transition-metal oxides.

[1] B. Müller, Mater. Corros. **53**, 789 (2002).

[2] M. C. Neves and T. Trindade, Thin Solid Films **406**, 93 (2002).

[3] M. Gotić, S. Musić, M. Ivanda, M. Šoufek, and S. Popović, J. Mol. Struct. **744–747**, 535 (2005).

[4] H. Golmojdeh and M. A. Zanjanchi, J. Electron. Mater. **43**, 528 (2014).

[5] I. C. Vinke, J. Diepgrond, B. A. Boukamp, K. J. de Vries, and A. J. Burggraaf, Solid State Ionics **57**, 83 (1992).

[6] L. Hoffart, U. Heider, L. Jörissen, R. A. Huggins, and W. Witschel, Solid State Ionics **72**, 195 (1994).

[7] J. D. Bierlein and A. W. Sleight, Solid State Commun. **16**, 69 (1975).

[8] A. Tücks and H. P. Beck, J. Solid State Chem. **178**, 1145 (2005).

[9] L. Hoffart, U. Heider, R. A. Huggins, W. Witschel, R. Jooss, and A. Lentz, Ionics **2**, 34 (1996).

[10] A. Kudo, K. Ueda, H. Kato, and I. Mikami, Catal. Lett. **53**, 229 (1998).

[11] R. L. Frost, D. A. Henry, M. L. Weier, and W. Martens, J. Raman Spectrosc. **37**, 722 (2006).

[12] A. Walsh, Y. Yan, M. N. Huda, M. M. Al-Jassim, and S.-H. Wei, Chem. Mater. **21**, 547 (2009).

[13] T. W. Kim and K.-S. Choi, Science **343**, 990 (2014).

[14] J. Su, L. Guo, N. Bao, and C. A. Grimes, Nano Lett. **11**, 1928 (2011).

[15] F. F. Abdi, N. Firet, and R. van de Krol, Chem. Catal. Chem. **5**, 490 (2013).

[16] J. A. Seabold, K. Zhu, and N. R. Neale, Phys. Chem. Chem. Phys. **16**, 1121 (2014).

[17] A. J. E. Rettie, W. D. Chemelewski, D. Emin, and C. B. Mullins, J. Phys. Chem. Lett. **7**, 471 (2016).

[18] A. J. E. Rettie, W. D. Chemelewski, J. Lindemuth, J. S. McCloy, L. G. Marshall, J. Zhou, D. Emin, and C. B. Mullins, Appl. Phys. Lett. **106**, 022106 (2015).

[19] A. Kudo, K. Omori, and H. Kato, J. Am. Chem. Soc. **121**, 11459 (1999).

[20] X. Zhang, Z. Ai, F. Jia, L. Zhang, X. Fan, and Z. Zou, Mater. Chem. Phys. **103**, 162 (2007).

[21] S. M. Thalluri, S. Hernández, S. Bensaid, G. Saracco, and N. Russo, Appl. Catal. B **180**, 630 (2016).

[22] Z. Zhao, Z. Li, and Z. Zou, Phys. Chem. Chem. Phys. **13**, 4746 (2011).

[23] V. Jovic, J. Laverock, A. J. E. Rettie, J.-S. Zhou, C. B. Mullins, V. R. Singh, B. Lamoureux, D. Wilson, T.-Y. Su, B. Jovic, H. Bluhm, T. Söhnelab, and K. E. Smith, J. Mater. Chem. A **3**, 23743 (2015).

[24] S. Tokunaga, H. Kato, and A. Kudo, Chem. Mater. **13**, 4624 (2001).

[25] H. Fan, T. Jiang, H. Li, D. Wang, L. Wang, J. Zhai, D. He, P. Wang, and T. Xie, J. Phys. Chem. C **116**, 2425 (2012).

[26] P. Yang, H. Liu, Z. Chen, L. Chen, and J. Wang, J. Appl. Crystallogr. **47**, 402 (2014).

[27] D. E. Cox and A. W. Sleight, Acta Crystallogr. B **35**, 1 (1979).

[28] A. J. E. Rettie, S. Mozaffari, M. D. McDaniel, K. N. Pearson, J. G. Ekerdt, J. T. Markert, and C. B. Mullins, J. Phys. Chem. C **118**, 26543 (2014).

[29] Z. Chen, S. Prosandeev, Z. L. Luo, W. Ren, Y. Qi, C. W. Huang, Lu You, C. Gao, I. A. Kornev, T. Wu, J. Wang, P. Yang, T. Sritharan, L. Bellaiche, and L. Chen, Phys. Rev. B **84**, 094116 (2011).

[30] X. Yu, O. Wilhelmi, H. O. Moser, S. V. Vidyaraj, X. Gao, A. T. Wee, T. Nyunt, H. Qian, and H. Zheng, J. Electron. Spectrosc. Relat. Phenom. **144**, 1031 (2005).

[31] X. Yin, M. A. Majidi, X. Chi, P. Ren, L. You, N. Palina, X. Yu, C. Diao, D. Schmidt, B. Wang, P. Yang, M. B. H. Breese, J. Wang, and A. Rusydi, NPG Asia Mater **7**, e196 (2015).

[32] G. Kresse and J. Hafner, Phys. Rev. B **48**, 13115 (1993).

[33] G. Kresse and J. Hafner, Phys. Rev. B **47**, 558 (1993).

[34] J. P. Perdew, K. Burke, and M. Ernzerhof, Phys. Rev. Lett. **77**, 3865 (1996).

[35] P. E. Blöchl, Phys. Rev. B **50**, 17953 (1994).

[36] V. I. Anisimov, J. Zaanen, and O. K. Andersen, Phys. Rev. B **44**, 943 (1991).

[37] J. K. Cooper, S. Gul, F. M. Toma, L. Chen, P.-A. Glans, J. Guo, J. W. Ager, J. Yano, and I. D. Sharp, Chem. Mater. **26**, 5365 (2014).

[38] F. M. F. de Groot, J. C. Fuggle, B. T. Thole, and G. A. Sawatzky, Phys. Rev. B **41**, 928 (1990).

[39] B. T. Thole and G. van der Laan, Phys. Rev. B **38**, 3158 (1988).

[40] F. de Groot, Coord. Chem. Rev. **249**, 31 (2005).

[41] J. Laverock, A. R. H. Preston, B. Chen, J. McNulty, K. E. Smith, L. F. J. Piper, P.-A. Glans, J.-H. Guo, C. Marin, E. Janod, and V. Ta Phuoc, Phys. Rev. B **84**, 155103 (2011).

[42] K. E. Kweon, G. S. Hwang, J. Kim, S. Kim, and S. Kim, Phys. Chem. Chem. Phys. **17**, 256 (2015).

[43] J. K. Cooper, S. Gul, F. M. Toma, L. Chen, Y.-S. Liu, J. Guo, J. W. Ager, J. Yano, and I. D. Sharp, J. Phys. Chem. C **119**, 2969 (2015).

[44] G. van der Laan, Phys. Rev. B **41**, 12366 (1990).

[45] L. R. De Jesus, G. A. Horrocks, Y. Liang, A. Parija, C. Jaye, L. Wangoh, J. Wang, D. A. Fischer, L. F. J. Piper, D. Prendergast, and S. Banerjee, Nat. Commun. **7**, 12022 (2016).

[46] M. Setvin, C. Franchini, X. Hao, M. Schmid, A. Janotti, M. Kaltak, C. G. Van de Walle, G. Kresse, and U. Diebold, Phys. Rev. Lett. **113**, 086402 (2014).

[47] A. Rusydi, R. Rauer, G. Neuber, M. Bastjan, I. Mahns, S. Müller, P. Saichu, B. Schulz, S. G. Singer, A. I. Lichtenstein, D. Qi, X. Gao, X. Yu, A. T. S. Wee, G. Stryganyuk, K. Dörr, G. A. Sawatzky, S. L. Cooper, and M. Rübhausen, Phys. Rev. B **78**, 125110 (2008).

[48] A. J. E. Rettie, H. C. Lee, L. G. Marshall, J. F. Lin, C. Capan, J. Lindemuth, J. S. McCloy, J. Zhou, A. J. Bard, and C. B. Mullins, J. Am. Chem. Soc. **135**, 11389 (2013).